

# Visualising and Quantifying Vapour Clouds with Interferometry

Sam Dehaeck<sup>1,\*</sup>, Alexey Rednikov<sup>1</sup>, Pierre Colinet<sup>1</sup>

<sup>1</sup>Transfers, Interfaces and Processes (TIPs) Department, Université Libre de Bruxelles, CP 165/67, Avenue F.D.  
Roosevelt 50, 1000 Brussels, Belgium.

\*corresponding author: sam.dehaeck@gmail.com

**Abstract** In the current work, digital holographic interferometry is used to measure the vapour concentration field surrounding evaporating liquids. This integrated measurement can be used to reconstruct the full 3D vapour concentration field in the case of an axisymmetric or 2D field. As an example for the axisymmetric reconstruction, an evaporating deposited droplet is analysed. From this we will demonstrate how one can extract the local evaporation rate and local temperature all along the liquid interface. In addition, three ways of obtaining the global evaporation rate are also applied which all give the same result, thus validating the vapour concentration measurements. This work was recently published in Langmuir [1]. For the 2D field, the concentration field inside a cuvette is measured and compared favorably to the predicted (Stefan-flow modified) field.

**Keywords:** Vapour Concentration, Evaporation, Interferometry, Local Evaporation Rate

## 1 Introduction

In this presentation we will show how interferometry can be used as a powerful instrument to visualise and characterise evaporation processes. As a liquid is evaporating, vapour is generated at the interface which will need to be evacuated either by diffusion or by (forced) convection in order to sustain the evaporation rate. Now as this evacuation rate is often the limiting step for freely evaporating liquids, much can be gained by investigating the vapour cloud. However, quantifying the local vapour concentration is something not a lot of techniques are capable of doing. In the past, measurements have been obtained by using the fluorescent properties of acetone (in liquid and gaseous form) (e.g. [2, 3, 4, 5]) and through Infrared absorption measurements [6]. Now, while these techniques are capable of showing the global shape of the vapour cloud, so far they have not been able to deliver data close to the liquid interface.

Previously, [7] used interferometry to measure the vapour concentration field surrounding an evaporating droplet and was able to extract interfacial temperatures of the droplet from the measurement of the vapour concentration at the interface. However, they did not continue to measure the local evaporation rate nor the extraction of the global evaporation rate from these measurements. In the present contribution, we will revisit this technique and show that it is now capable of delivering much more information about the evaporating liquid. This work has been published in [8, 9, 1, 10].

For evaporating liquid inside a cuvette, the full reconstruction is even easier and here we will demonstrate the good correspondance between our measured concentration profiles and the theoretically predicted concentration field.

## 2 Droplet Vapour Cloud

### 2.1 Obtaining the vapour mole fraction field

For the droplet experiment, a simple Mach-Zehnder interferometer is used such as the one shown in Figure 1. A droplet of 3M<sup>TM</sup> Novec<sup>TM</sup> HFE-7000 is deposited at the bottom of a silicon wafer. This hanging droplet (the

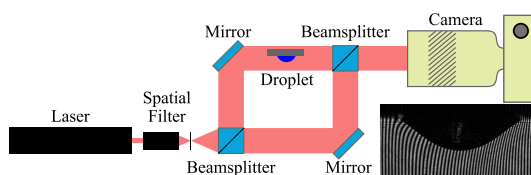


Fig. 1 Experimental set-up and typical raw image

black object in the shown raw image) is left to evaporate in the ambient air, while shielding it from draughts. Before the deposition of the drop, the interferometer is set to generate a homogeneous system of vertical fringes. At this time a first image is acquired, which is used as a pixel-wise calibration for which the refractive index is known to be homogeneous and equal to that of pure air. Then the drop is deposited and the fringes are distorted by the presence of the vapour cloud surrounding the droplet, which itself appears black in the image. This image is analysed to yield the phase shift at each pixel by the Fourier Transform Profilometry algorithm described by [11]. This phase is then compared to the reference phase obtained for that pixel in the previously mentioned reference/calibration image (as detailed in [12]). This then yields the total phase shift for that pixel. However, the information obtained in this way is 'wrapped', which means that the phase shift image ranges from 0 to  $2\pi$ . Next step is the so-called 'unwrapping' of this image by the algorithm described by [13] resulting in a map of the total phase shift for each pixel.

This phase map is proportional to the optical path length difference between the object and the reference beam. In order to convert this into a refractive index field, a tomographic reconstruction step is required as our measurement has integrated the local refractive index field along a line of sight. As the present subject is axisymmetric, this reconstruction can be done based on a single image and using the inverse Abel transform (e.g. [14]). Inherent to this transform is a certain augmentation of the noise, especially near the symmetry axis. As such, many of the algorithms proposed over the years (such as the one by [15]) add a certain filtering capability to alleviate these problems. We have implemented three different algorithms in order to ascertain which one could give the best results in our particular case: the three-point Abel transform method by [14], the Modified Fourier-Hankel (MFH) method by [15] and the Even-Power (EP) method by [16]. The preliminary scan of these three algorithms has shown that all methods give essentially the same results. However, with the aim of extracting local gradients, the smooth result from the EP-method is preferred for the present work.

The final step is then to transform this 3D refractive index field into the vapour concentration field  $\chi$ . From the Lorentz-Lorenz equation (e.g. [17, 18]), it is known that the refractive index of a mixture of gases ( $n \approx 1$ ) can be expressed as

$$n_{\text{mix}} - 1 = \frac{3P_{\text{tot}}}{2\mathcal{R}T} \sum_i \chi_i A_i, \quad (1)$$

where  $n_{\text{mix}}$  is the refractive index of the mixture,  $P_{\text{tot}}$  is the total ambient pressure,  $\mathcal{R}$  the universal gas constant,  $T$  the temperature,  $\chi_i$  is the mole fraction of the component  $i$  and  $A_i$  is the molecular polarisability of the component  $i$ . Treating the gas as a binary mixture of air and HFE-7000 vapour, we can develop this formula to the following form when temperature gradient influences on the refractive index are neglected with respect to concentration changes:

$$\chi = \frac{\Delta n}{n_{\text{HFE}} - n_{\text{air}}}. \quad (2)$$

Thus, a simple proportionality relation between the refractive index difference field and the mole fraction field is found. A posteriori we have calculated that neglecting the temperature influence introduces at most an error of 3% in the present vapour mole fraction fields.

In Figure 2, the measured concentration field surrounding the evaporating droplet is shown together with two iso-concentration lines. This configuration is completely different from the pure diffusional field anticipated which would yield circular isoconcentration lines centred on the droplet centre. This is due to the presence of natural convection which makes the heavy vapour mixture at the interface (approximately 4 times heavier than regular air) fall down in a plume. The presence of such convection in the vapour phase is neglected in many of the papers dealing with evaporating droplets (e.g. [19]), but has recently been shown by Kelly-Zion et al. ([20, 21]) to be present also in sessile droplets where it can significantly enhance the global evaporation rate. In the present configuration, we have also found that the global evaporation rate is increased by a factor 4 for a droplet of 2mm radius and we will show for the first time what the influence is on the local evaporation rate distribution.

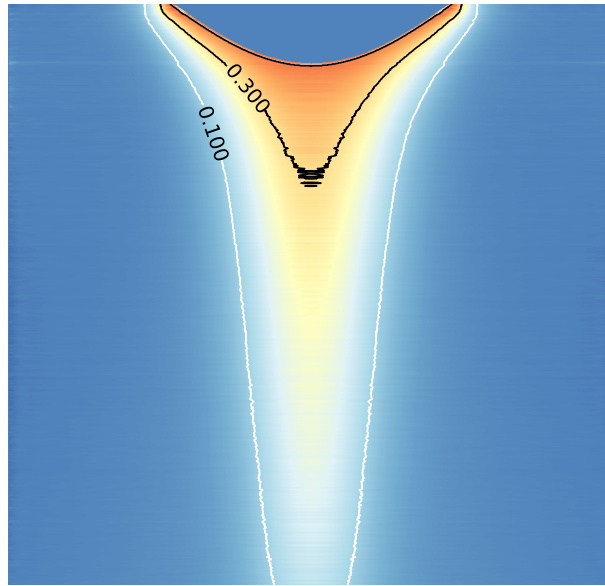


Fig. 2 Vapour concentration field measured around an evaporating droplet with radius 1.81mm.

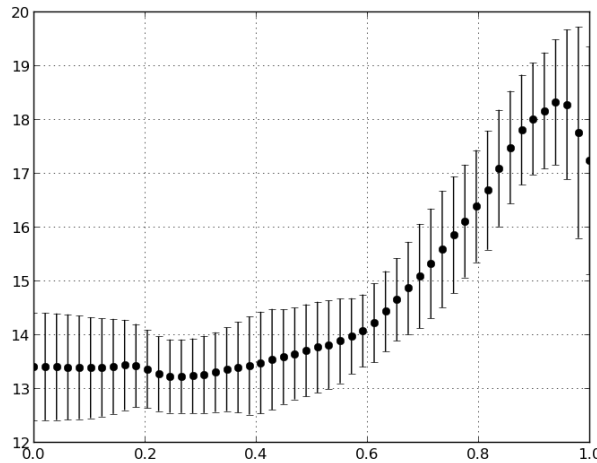


Fig. 3 Interfacial temperature versus non-dimensional position of an evaporating droplet with radius 1.81mm.

## 2.2 Interfacial temperature determination

Now as was already shown by [22], one can obtain a measurement of the interfacial droplet temperature by extracting the mole fraction at the interface of the drop. Assuming chemical equilibrium at the interface implies that the local temperature and the local vapour mole fraction are linked by the known saturation-pressure data (or simply the Clausius-Clapeyron relation). This brings a second equation to the table, which allows us, at the liquid interface, to take into account the effect of temperature variations on the refractive index field.

In Figure 3, the measured interfacial temperature is shown as a function of the non-dimensional location  $r$  for a droplet with radius 1.81mm. This goes from the center of the drop ( $r = 0$ ) up to the contact line ( $r = 1$ ). This shows that the temperature is much smaller in the center of the drop than at the contact line. At the contact line this temperature should in theory go back to the ambient temperature (i.e. 24°C) due to the good conductivity of the substrate but experimentally this is not recovered. However, as is demonstrated in [1], this is probably a limitation of our tomographic reconstruction technique which smooths out the large gradients present at the contact line and is hence underestimating the concentration at the contact line. When going further away from the contact line, the interfacial temperature drops sharply due to the fact that the necessary heat supply through the liquid phase becomes more difficult.

This sharp drop in interfacial temperature leads to a very intense change in interfacial tension along the

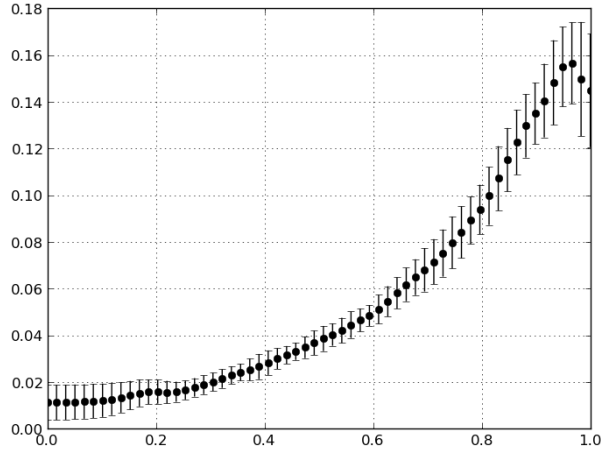


Fig. 4 Local evaporation rate versus non-dimensional position of an evaporating droplet with radius 1.81mm.

droplet interface. This creates a so-called Marangoni flow inside the droplet. Numerical simulations not shown here, have demonstrated that this Marangoni flow can reach velocities inside the droplet of up to 5 cm/s [1]. This speed is so large, it even has a marked impact on the convection of the vapour cloud. As the interfacial motion is directed towards the cold point (i.e. the centre) and the general motion in the vapour cloud is also in this direction, the Marangoni flow leads to an acceleration of the vapour evacuation and hence an intensification of the evaporation rate, which numerically was shown to be up to 30%.

### 2.3 Local evaporation rate determination

Next to the interfacial mole fraction  $\chi_\sigma$ , one also needs to calculate the local gradient of the mole fraction along a normal to the droplet interface ( $\left. \frac{\partial \chi}{\partial n} \right|_\sigma$ ) so as to be able to measure the local evaporation rate  $J_{l,\text{surf}}$  through the following formula:

$$J_{l,\text{surf}} = - \frac{M_v P_{\text{tot}} D_v}{\mathcal{R} T (1 - \chi_\sigma)} \left. \frac{\partial \chi}{\partial n} \right|_\sigma \quad (3)$$

with  $M_v$  the molar weight of the vapour (0.2kg/mol),  $P_{\text{tot}}$  the total (atmospheric) pressure,  $D_v$  the diffusion coefficient of the vapour-air mixture ( $8.11 \times 10^{-6} \text{ m}^2/\text{s}$ ) obtained by independent Stefan-tube experiments,  $\mathcal{R}$  the universal gas constant (8.31J/molK),  $T$  the temperature,  $\chi_\sigma$  the mole fraction at the interface (see above) and  $\left. \frac{\partial \chi}{\partial n} \right|_\sigma$  the normal mole fraction gradient at the interface. As spatial variations of the gas pressure are expected to be thermodynamically negligible, we take  $P_{\text{tot}} = P_{\text{amb}}$ . On the other hand, given that the corresponding effect is anyway not taken into account e.g. in the refractive-index calibration away from the interface, it is consistent to set  $T = T_{\text{amb}}$  in eq 3 too and to evaluate  $D_v$  just at  $T_{\text{amb}}$ .

The resulting local evaporation rate measurement is shown in Figure 4. This shows indeed that the local evaporation rate increases dramatically when approaching the contact line. This together with the larger area associated with the contact line with respect to the centre of the drop, leads to a significantly larger evaporation rate for the contact line region than for the centre of the drop. We remark here that the local evaporation rate is not seen to diverge for  $r \rightarrow 1$  as is theoretically the case for the pure diffusion regime (see e.g. [23] or [24]). But again this is expected, due to the tomographic reconstruction step which smooths out the large gradients expected in that case. Note that this measurement can also easily be transformed into a local heat sink by multiplying with the latent heat. Possibly neglecting the heat supply through the vapour, it is then possible to simulate numerically the mass and heat transport inside the droplet. This is important in order to estimate the deposition pattern present inside the droplet, or the thermal load on the substrate.

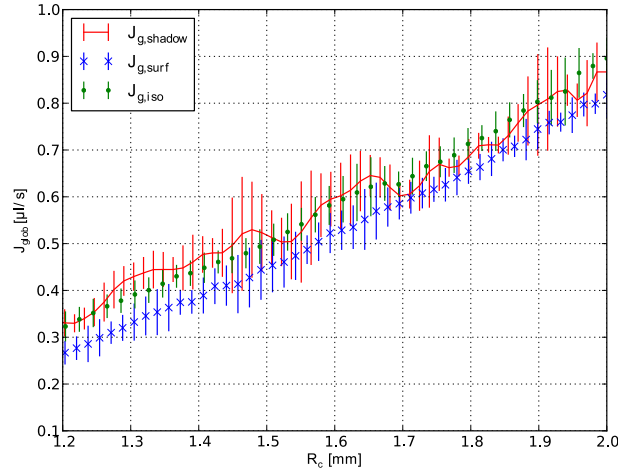


Fig. 5 Global evaporation rate versus droplet radius.

## 2.4 Global evaporation rate determination

From our images, there are three ways to determine the global evaporation rate. The simplest one is simply by measuring the evolution in time of the droplet interface from its shadow. As this is a standard way of measuring the global evaporation rate, it will be used as the validating measurement here. The second approach is by integrating the above-determined local evaporation rates over the surface of the drop. Thus, the following integration is performed with  $h'$  the radial derivative of the local thickness of the drop and  $R_c$  its contact radius:

$$J_{g,\text{surf}} = \int_0^{R_c} 2\pi r \sqrt{1 + h'^2} J_{l,\text{surf}} dr. \quad (4)$$

As the normal gradient at the contact line is eventually infinite and because the profile fitting of the drop is subject to some uncertainty, a second method using the iso-concentration lines was also developed to avoid this source of imprecision. Although the derivation of the formula is not performed here (see our upcoming article in Langmuir), it turns out that the following integration along an iso-concentration line also leads to the global evaporation rate:

$$J_{g,\text{iso}} = -\frac{M_v P_{\text{amb}} D_v}{\mathcal{R} T_{\text{amb}} (1 - \chi_{\text{iso}})} \int \left. \frac{\partial \chi}{\partial n} \right|_{\text{iso}} dS_{\text{iso}}. \quad (5)$$

A clear advantage of this approach is that the estimation can be performed at multiple iso-concentration lines and averaged in order to obtain a more accurate measurement. Additionally, this approach can even be performed when the liquid interface is not clearly visible (too small or too flat) or when the resolution/precision near the interface is not large enough (such as is the case for PLIF measurements due to the halation effect). An advantage of both techniques with respect to traditional measurement techniques based on backlighting or gravimetric methods is that both of the vapour-based global evaporation rate measurement techniques are instantaneous.

The comparison of the three mentioned methods is shown in Figure 5. For the side view shadow measurement, the derivative with respect to time was taken and averaged over multiple images (up to 30). Nevertheless, this side view measurement remains very noisy. As mentioned before, the vapour-based measurements are instantaneous and also less noisy. Nevertheless, the same results are obtained thus validating in some sense our local evaporation rates extracted previously.

## 3 Cuvette Vapour Cloud

For this experiment, some HFE-7000 was poured into a small glass container with (internal) dimensions 50x50x50mm. This cuvette was then placed into the same interferometer as shown in Figure 1. In the same

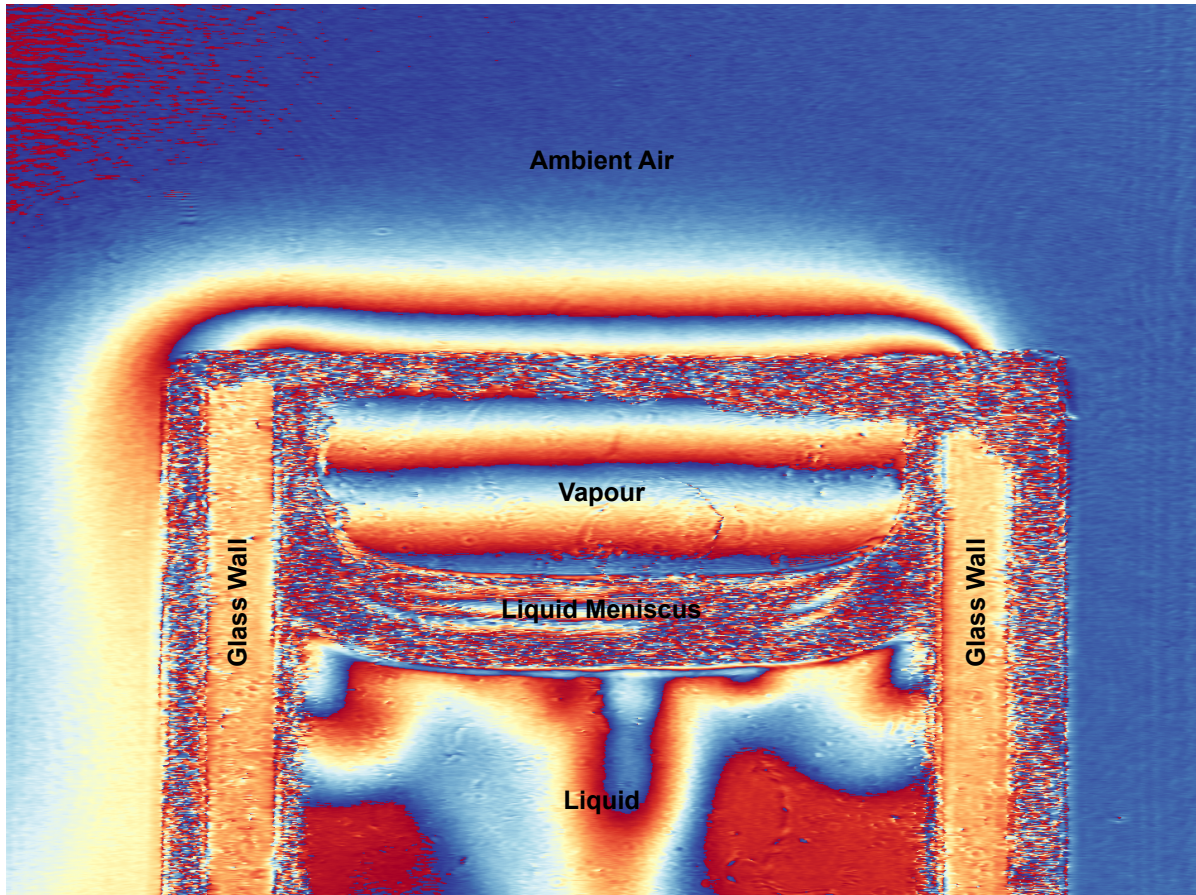


Fig. 6 Global vapour cloud inside a glass container

manner as described in subsection 2.1, in each pixel of the image the phase shift with respect to the reference case (cuvette without liquid) is extracted. This phase shift image  $\Delta\phi$  is converted directly to the refractive index profile as the integration path is now constant when assuming no vapour concentration variations outside of the cuvette. This is obtained through the following formula:

$$\Delta n = \frac{\lambda \Delta\phi}{2\pi t}$$

with  $t$  the thickness of the cuvette (50mm). As before, this refractive index field is simply proportional to the concentration profile. A typical image obtained for the case when a lot of liquid is poured into the container is shown in Figure 6, which was extracted from the video in [8]. Note the phase jumps from 0 to  $2\pi$  in the vapour cloud (blue $\leftrightarrow$ red jumps). In the vapour cloud close to the meniscus, we note that these lines are horizontal denoting the isoconcentration lines. However, when coming outside of the cuvette (above the noisy region), the vapour cloud extents for only a centimeter and then the vapour is flowing downwards along the sides. This is again due to the fact that the vapour is heavier than the surrounding air and natural convection sweeps it downwards. Also note that in the shown experiment, temperature variations in the liquid due to evaporative cooling induce visible refractive index differences. In the present experiments however, the height of the liquid layers was only a couple of millimetres in order to limit temperature variations in the liquid.

The measured concentration profile could be compared to the theoretically predicted concentration field including the Stefan flow effect in a diffusion tube. In view of essential vapour mole fractions, this effect needs to be taken into account. The general formula is as follows:

$$h = H \left[ 1 - \frac{\ln(1 - \chi)}{\ln(1 - \chi\sigma)} \right]$$

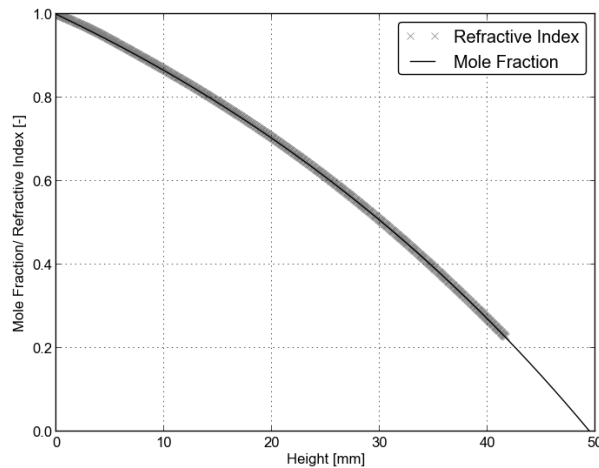


Fig. 7 Comparison adimensional experimental refractive index profile vs adimensional concentration profile for evaporating liquid in a cuvette.

Here,  $h$  is the height measured starting from the liquid,  $H$  is the height at which the vapour mole fraction reaches zero,  $\chi$  is the vapour mole fraction of vapour at location  $h$  and  $\chi_\sigma$  is the vapour mole fraction at the interface. In general, for this kind of theoretical approach, the location  $H$  at which the concentration reaches zero is known from the construction of the diffusion tube. In the present application it can be seen that it is close to the height of the cuvette but not quite. Therefore, this height  $H$  is used as a fitting parameter. Unfortunately a second fitting parameter is also required, which is the mole fraction at the liquid interface. This due to two effects. First, the liquid meniscus along the borders prevents us from measuring the vapour concentration precisely at the interface but only some distance away from it. Second, the glass bottom wall combined with the thermal insulation qualities of the liquid leads to a situation where the evaporative cooling can reduce the temperature of the liquid interface considerably before the diffusion profile is fully established and measured (after 200s). As such the mole fraction at the interface  $\chi_\sigma$  is the second fitting constant. In Figure 7, the comparison of the adimensional refractive index profile and the adimensional mole fraction profile is shown. As can be seen, both profiles are in excellent agreement. While the current configuration with two fitting constants is not perfect, such a configuration could be used for instance to measure the refractive index of different vapours.

#### 4 Conclusions

As the results have shown, digital holographic interferometry is capable of measuring the vapour concentration field surrounding evaporating liquids. For the case of evaporating droplets, we were able to obtain the absolute interfacial temperature field, the local evaporation rate distribution and finally also at least two different instantaneous global evaporation rate measurements. Essentially all the critical parameters governing the evaporation process can be obtained from a single laser and camera set-up and tracked at any frame rate. We also measured the vapour concentration profile inside a glass container and compared it favourably to the theoretical prediction.

#### References

- [1] S. Dehaeck, A. Rednikov, and P. Colinet. Vapor-based interferometric measurement of local evaporation rate and interfacial temperature of evaporating droplets. *Langmuir*, 30(8):2002–2008, 2014.
- [2] R. Bazile and D. Stepowski. Measurements of vaporized and liquid fuel concentration fields in a burning spray jet of acetone using planar laser induced fluorescence. *Exp. Fluids*, 20:1–9, 1995.
- [3] M.C. Thurber and R.K. Hanson. Simultaneous imaging of temperature and mole fraction using acetone planar laser-induced fluorescence. *Exp. Fluids*, 30:93–101, 2001.

- [4] Y. Hardalupas, S. Sahu, and A.M.K.P. Taylor. Measurement of vapour concentration and droplet size and velocity in an evaporative spray, 15th int symp on applications of laser techniques to fluid mechanics. In *15th Int Symp on Applications of Laser techniques to fluid mechanics*, Lisbon, Portugal, 2010.
- [5] A. Charogiannis and F. Beyrau. Laser induced phosphorescence imaging for the investigation of evaporating liquid flows. *Exp. Fluids*, 54:1518, 2013.
- [6] P.L. Kelly-Zion, C.J. Pursell, N. Hasbammer, B. Cardozo, K. Gaughan, and K. Nickels. Vapor distribution above an evaporating sessile drop. *Int. J. Heat and Mass Transfer*, 65:165–172, 2013.
- [7] G.R. Toker and J. Stricker. Holographic study of suspended vaporizing volatile liquid droplets in still air. *Int. J. Heat and Mass Transfer*, 39(16):3475–3482, 1996.
- [8] S. Dehaeck and P. Colinet. Vapour cloud dynamics induced by evaporation. *arXiv*, 1010.3258, 2010.
- [9] S Dehaeck, Y. Tsoumpas, and P. Colinet. Analyzing droplets through digital holography and a 1d wavelet transform technique. In *Digital Holography and Three-Dimensional Imaging, OSA Technical Digest*, page DW3A.5., April 2013.
- [10] S Dehaeck, A. Rednikov, and P. Colinet. Measuring the local and global evaporation rate of fast evaporating droplets with interferometry. In *17th International Symposium on Application of Laser Techniques to Fluid Mechanics*, Lisbon, 7-10 July 2014.
- [11] M. Takeda, H. Ina, and S. Kobayashi. Fourier-transform method of fringe-pattern analysis for computer-based tomography and interferometry. *J. Opt. Soc. Am.*, 72:156–160, 1982.
- [12] T Kreis. Digital holographic interference-phase measurement using the fourier-transform method. *JOSA A*, 3(6):847–855, 1986.
- [13] M. A. Herraes, D. R. Burton, M. J. Lalor, and M. A. Gdeisat. A fast two-dimensional phase unwrapping algorithm based on sorting by reliability following a non-continuous path. *Applied Optics*, 41:7437–7444, 2002.
- [14] C.J. Dasch. One-dimensional tomography: a comparison of Abel, onion-peeling, and filtered backprojection methods. *Applied Optics*, 31(8):1146–1152, 1992.
- [15] S. Ma, H. Gao, and L. Wu. Modified Fourier-Hankel method based on analysis of errors in Abel inversion using Fourier transform techniques. *Applied Optics*, 47(9):1350–1357, 2008.
- [16] M. El Fagrigh and H. Chehouani. A simple Abel inversion method of interferometric data for temperature measurement in axisymmetric medium. *Optics and Lasers in Engineering*, 50:336–344, 2012.
- [17] L.R. Pendrill. Refractometry and gas density. *Metrologia*, 41:S40–S51, 2004.
- [18] A. Borzsonyi, Z. Heiner, M. P. Kalashnikov, A. P. Kovacs, and K. Osvay. Dispersion measurement of inert gases and gas mixtures at 800 nm. *Applied Optics*, 47(27):4856–4863, 2008.
- [19] R.D. Deegan, O. Bakajin, T.F. Dupont, G. Huber, S.R. Nagel, and T.A. Witten. Contact line deposits in an evaporating drop. *Phys. Rev. E*, 62:756–765, 2000.
- [20] P. L. Kelly-Zion, C.J. Pursell, R.S. Booth, and A.N. Van Tilburg. Evaporation rates of pure hydrocarbon liquids under the influences of natural convection and diffusion. *Int. J. Heat and Mass Transfer*, 52:3305–3313, 2009.
- [21] P.L. Kelly-Zion, C.J. Pursell, S. Vaidya, and J. Batra. Evaporation of sessile drops under combined diffusion and natural convection. *Colloids Surf., A*, 381:31–36, 2011.
- [22] G.R. Toker and J. Stricker. Study of suspended vaporizing volatile liquid droplets by an enhanced sensitivity holographic technique : additional results. *Int. J. Heat and Mass Transfer*, 41(16):2553–2555, 1998.
- [23] R.D. Deegan, O. Bakajin, T.F. Dupont, G. Huber, S.R. Nagel, and T.A. Witten. Capillary flow as the cause of ring stains from dried liquid drops. *Nature*, 389:827–829, 1997.
- [24] Y.O. Popov. Evaporative deposition patterns: Spatial dimensions of the deposit. *Phys. Rev. E*, 71:036313, 2005.